JOURNAL OF AIRCRAFT
Vol. 41, No. 1, January–February 2004

Aeroelastic Optimization of Adaptive Bumps for Yaw Control

Anand Natarajan,* Rakesh K. Kapania,† and Daniel J. Inman‡
Virginia Polytechnic Institute and State University, Blacksburg, Virginia 24061-0203

This paper captures the aeroelastic behavior of adaptable bumps on morphing wings using trained neural networks. Parameters of the bump such as the height, size, location, and shape play a major aerodynamic and structural role. Though other issues such as wave drag minimization, boundary layer control are discussed, the primary problem addressed here is the generation of the lateral directional moment. The shape of the bump is optimized so that it produces maximum yaw moment with a minimum actuation energy spent in creating the adaptive bump. The analysis of fluid separation on the airfoil surface due to various types of bumps and its effects on the aerodynamic forces is performed using the computational fluid dynamics (CFD) software FLUENT™. This analysis is performed at a low speed of Mach 0.3 and at a transonic speed of Mach 0.7. Structural analysis is performed using the finite element software ANSYS™ using a nonlinear beam model of the bump. In order to perform an aeroelastic analysis, the softwares FLUENT and ANSYS have to be interconnected so that the changing aerodynamic pressure with bump deformation is reflected in the structural analysis. Direct coupling of two such numerical codes, one based on CFD and the other based on finite element modeling (FEM), is computationally expensive. Hence, artificial neural networks are trained from these aerodynamic and structural analysis. Two neural networks are trained, one for the aerodynamic pressure and the other for the structural loads and strain energy. These two neural networks serve as an efficient decoupler, that facilitates an aeroelastic optimization procedure to evaluate the best bump shape for maximum drag for providing micro-yaw control while using the minimum actuation energy and minimizing the loss in the lift.

Nomenclature

AR	=	aspect ratio
b	=	wing half-span
C_n	=	coefficient of yaw moment
c	=	sectional chord length
c_d	=	sectional drag coefficient
c_l	=	sectional lift coefficient
G_i	=	penalty functions
J	=	Jacobian
k	=	turbulent kinetic energy
u	=	velocity in x direction
v	=	velocity in y direction
ϵ	=	dissipation of kinetic energy
κ	=	curvature
μ_t	=	turbulent viscosity
ρ	=	density of air
τ	=	fluid stress

Introduction

BECAUSE of the growth of research in smart materials, there has been a keen interest in the application of these materials to aircraft wings to obtain a better performance in off-design conditions.[1,2] Adaptive surfaces have been employed in fighter aircraft for effectively changing the leading- and trailing-edge cambers in flight.[3] This has eliminated sudden pressure jumps due to discontinuous surfaces such as slats and flaps on the wing. Recently, it was shown[4] that the variable camber trailing edge can prevent roll reversal from occurring at flight speeds where the traditional ailerons are no longer effective. Considerable research in Europe has been performed toward effectively using adaptable surfaces in wings. For example, the extent of flow control over the wing, that can be achieved using the adaptive nature of the wing, has been a subject of much research.[5] The use of adaptive materials for forming spoiler bumps in controlling shock location and reducing wave drag is another major research initiative.[6]

Morphing a wing, constitutes deforming the wing surface at localized regions and/or changing the wing twist, section camber in flight. Because such deformations are brought about by actuators that may be able to generate only small forces, the wing surface must be flexible enough to allow needed deformations. At the same time, we require that the wing withstand the aerodynamic loads. The deformation of such flexible wings in a freestream requires an aeroelastic analysis to predict the actuator loads.

Recent research has focused on the use of morphing wings for unmanned combat air vehicles (UCAV).[7] UCAVs are tailless aircraft, and hence, their lateral directional motion control is very important. All-wing aircraft such as the YB-49 use drag rudders for roll control and to eliminate adverse yaw.[8] The concept of the drag rudder started from the need to eliminate vertical surfaces from the aircraft because 1) vertical surfaces violated the all-wing aircraft principle.[9] and 2) vertical surfaces increase the aircraft radar signature. These split flaps on the wing when deflected, cause localized flow separation and cause vortices that increase the drag on that wing. The increased drag on one wing will produce a yawing moment on the aircraft. There are many issues associated with this, namely, the magnitude of the yawing moment and the stability of the aircraft. The location of the split flap can sometimes produce an adverse side force, thus, canceling a significant part of the yawing moment.[10] Because flaps are separate physical entities, their locations on the wing cannot be changed in flight. To have effective yaw control and, hence, roll control, it would be highly advantageous to change the position of the drag rudder in flight and also to be able to provide greater sensitivity to the flow control. Toward this goal, the application of adaptive materials to aircraft wings is beneficial. Usually, spoilers are located around midchord or farther downstream. Here, we investigate placing the spoiler close to the leading edge. This is not unusual. Cole[11] describes flutter control of a rectangular

Presented as Paper 2002-0707 at the Aeroelastic Analysis of Adaptable Bumps Used as Drag Rudders, Reno, Nevada, 15 January 2002; received 14 January 2003; revision received 30 April 2003; accepted for publication 16 June 2003.

*Graduate Research Assistant, Department of Aerospace and Ocean Engineering.
†Professor, Department of Aerospace and Ocean Engineering. Associate Fellow AIAA.
‡G.R. Goodson Professor, Department of Mechanical Engineering; Director, Center for Intelligent Material Systems and Structures. Fellow AIAA.

wing with spoilers placed at 10% of the chord. Here, we propose to use bumps on the airfoil surface to generate drag to achieve yaw control.

The actuator energy required in generating a bump is a critical issue because the changing aerodynamic forces require the actuator to perform differently in different scenarios. Boundary-layer control through an adaptive leading-edge bump has been studied for the purpose of delaying the occurrence of stall.[12] The control of the position and shape of this adaptable bump was found to be a difficult task due to the rapidly changing aerodynamic loads. Pinkerton and Moses[12] concentrate on the use of the smart actuator THUNDER for creating these bumps and not on the aeroelastic analysis of the bumps. Herein, we shall study the deformation of these adaptable bumps through an aeroelastic analysis and also perform an optimization to decide on the best bump shape that will minimize the actuation energy and loss in lift and at the same time provide sufficient drag to cause a yawing motion of the aircraft. To achieve this, a computational fluid dynamics (CFD) model is coupled to a finite element structural model of the bump. This coupling is achieved through the use of neural networks.

Neural networks allow for nonlinear surface fitting for multivariate interpolation problems, and hence, they are suitable for aeroelastic applications. Recent research work in fluid dynamics shows interesting applications of neural networks.[13,14] Herein we utilize neural networks to represent static nonlinear aeroelasticity.

Yaw Moment Generation

The change in drag over the wing due to a leading-edge bump will lead to a yaw moment. If two-dimensional aerodynamics is used to calculate the drag, then the yaw moment coefficient is defined by

$$C_n = \frac{1}{4b}\mathrm{AR}\int_{\beta}^{1} \Delta c_d c(\eta)\eta \, \mathrm{d}\eta \tag{1}$$

where η is the nondimensional span, AR is the wing aspect ratio, and b is the semiwing span. For the drag force to be effective, the bump must be located on the outboard wing, from the wing tip to a certain span distance β. Because the leading edge governs the formation of the boundary layer, the bump must be situated near the leading edge. The size, shape, and location of this bump is critical to the determination of the drag rise. Bauer[15] describes the yaw moments generated due to the presence of micro-drag generators on the top surface of the wing. Raney and Park[16] detail the effect of shape change arrays on an adaptable wing in producing yaw. These accounts indicate that a yaw moment coefficient of the order of 10^{-3} is adequate. Incorporating the wing geometry in Eq. (1) would then reveal the change in drag force required to obtain the desired yaw moment coefficient.

The usual practice for control of aircraft lateral dynamics is to use deflected spoilers. Spoilers separate flow by providing an obstacle to the boundary layer, whereas, the adaptive bumps separate flow by providing for an adverse pressure gradient. Therefore, the size of the bumps at the leading edge are much smaller compared to the width of a spoiler. In contrast, if the bump is provided at the trailing edge as an imitation of a spoiler, the size of the bump required to generate sufficient yaw moment would be too high, and hence, the actuation energy needed to create such a bump would be too high to be realistic.

Aerodynamic Model

The compressible Navier–Stokes equations are used to model the aerodynamics over the airfoil. These equations in two-dimensions are

$$\frac{\partial \boldsymbol{Q}}{\partial t} + \frac{\partial \boldsymbol{F}}{\partial x} + \frac{\partial \boldsymbol{G}}{\partial y} = \frac{\partial \boldsymbol{J}_x}{\partial x} + \frac{\partial \boldsymbol{J}_y}{\partial y} \tag{2}$$

where

$$\boldsymbol{Q} = \begin{pmatrix} \rho \\ \rho u \\ \rho v \\ \rho e \end{pmatrix}, \qquad \boldsymbol{F} = \begin{pmatrix} \rho u \\ \rho u^2 + p \\ \rho uv \\ \rho eu + pu \end{pmatrix}, \qquad \boldsymbol{G} = \begin{pmatrix} \rho p \\ \rho uv \\ \rho v^2 + p \\ \rho ve + pu \end{pmatrix}$$

$$\boldsymbol{J}_x = \begin{pmatrix} 0 \\ \tau_{xx} \\ \tau_{xy} \\ u\tau_{xx} + v\tau_{xy} + K_x \dfrac{\partial T}{\partial x} \end{pmatrix}$$

$$\boldsymbol{J}_y = \begin{pmatrix} 0 \\ \tau_{xy} \\ \tau_{yy} \\ K_y \dfrac{\partial T}{\partial y} + u\tau_{xy} + v\tau_{xy} \end{pmatrix}$$

The CFD software FLUENT™ is used for handling turbulence modeling and unsteady flows that result from separated boundary layers over the airfoil. Figure 1 shows the portion of the leading edge of the airfoil that is being deformed into a small bump. Initially, a large number of CFD calculations are performed using FLUENT for different bump shapes and sizes, the bump being always located just after the leading edge. The results of the CFD calculations indicate the pressure distribution over the bump, the drag, the lift, and the pitching moment over the airfoil. Since the calculation of aerodynamic forces over the airfoil for all bump sizes and shapes using CFD is a very time consuming and expensive task, the results obtained using FLUENT are utilized in training a neural network. Thus, all further aerodynamic effects of different bumps on the leading edge of the airfoil are calculated using the trained neural network and not FLUENT.

Figure 2 shows the computational grid, made around an 8% thick symmetric airfoil. The freestream is at an angle of attack of 5 deg. The freestream Mach number is set at either 0.3 or 0.7. This is because we consider only the low subsonic and lower transonic regimes. Using pressure far-field boundary conditions, a realizable k–ϵ turbulence model, and an implicit coupled solver, the fluid flow is modeled. Turbulence modeling is still an ongoing research activity in the fluid dynamics community. Hence, a perfect turbulence model does not exist. The k–ϵ model uses the Boussinesq hypothesis, wherein the turbulent stresses are expressed as the product of the isotropic eddy viscosity and the mean velocity strain rate. The standard k–ϵ model is valid only for fully turbulent flows at low

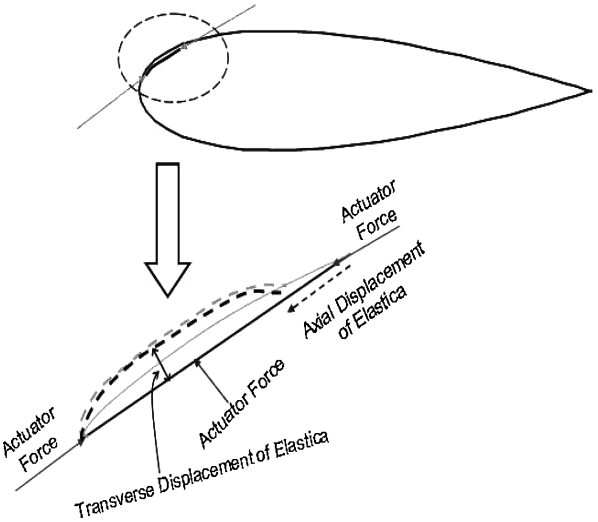

Fig. 1 Actuation mechanism for leading-edge bump.

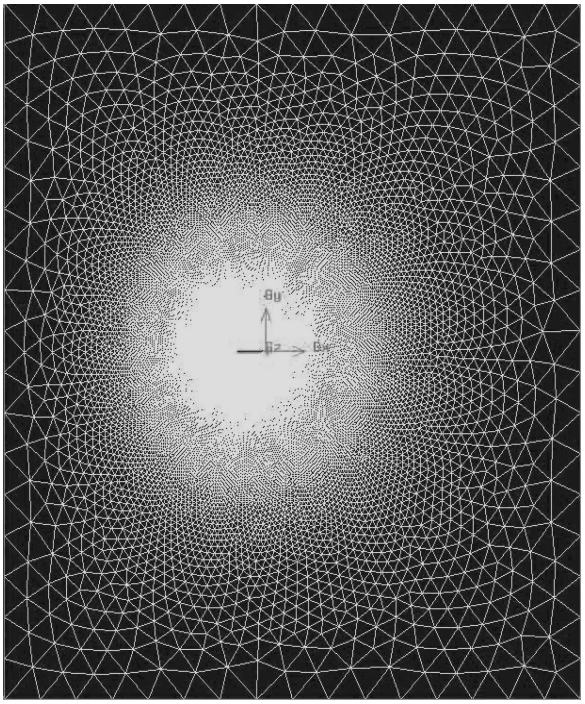

Fig. 2 Computational grid; triangular grid with pressure far-field boundary conditions at 10 times chord distance.

Reynolds number. However, a variation of the standard k–ϵ model is available in FLUENT and is used here. The Reynolds numbers of the current study based on an airfoil chord of 2.25 m is in the region of $1.5E07$. Because this is a high Reynold's number region, we use the realizable k–ϵ model as suggested by Shih et al.[17] Here the turbulent viscosity given by

$$\mu_t = \rho C_\mu (K^2/\epsilon) \tag{3}$$

is not a constant, where ϵ is the kinetic energy dissipation and C_μ is a variable model parameter.

The convergence limit is based on the convergence of the lift and drag forces, which converge to a certain value in the case of steady flow, that is, not much flow separation, or they oscillate about some mean value for unsteady flow (full flow separation). The airfoil is modeled using B-splines. The mesh representation of the airfoil must reflect the true leading-edge shape and the bump shape. Hence, the grid is extremely fine near the airfoil surface. To capture the effect of flow separation and possible subsequent reattachment, a grid refinement is done at the airfoil surface. The effect of the bump on the flow can be seen even before flow separation, by noting the boundary-layer thickness. Once a vortex shedding pattern emerges at the bump, the flow solver is switched from the steady solver to an unsteady implicit solver. Although the separated flow is unsteady and turbulent, it is not chaotic. There is a repeatability in the analysis with regard to the aerodynamic forces.

Structural Model

Minimum energy curves are a much researched topic in differential geometry (see Ref. 18). The problem states that for all curves of a fixed length between two endpoints, there is a unique curve subject to certain constraints that minimizes the curvature change along the span of the curve. This is a variational problem given as follows. Minimize

$$\Pi = \int_0^l \kappa(x)^2 \,\mathrm{d}x - G_0 \left[\int_0^l \sqrt{1 + \left(\frac{\mathrm{d}y}{\mathrm{d}x} \right)^2} \,\mathrm{d}x - l \right]^2 - \sum_{i=1}^{N} G_i (x_i - \alpha_i)^2 \tag{4}$$

where κ is the curvature of the curve, G_0 is the penalty function multiplying the fixed curve length constraint, and G_i are penalty functions multiplying any additional constraints $x_i - \alpha_i$. Structurally, the solution to the minimum-energy curve is obtained by studying the deformation of a pinned–pinned elastica. This elastica curve is obtained by applying horizontal forces greater than the Euler critical buckling load to the ends of the elastica. As shown in Fig. 1, under the airfoil skin a membrane is present, which is treated as a curved elastica. When the actuator forces are used as a means for buckling the elastica element, a bump is created on the airfoil surface. Vertical actuator forces to change the shape of the bump can also be present. This elastica shape is the minimum energy bump on the airfoil surface for a specified bump height and size. However, this bump will not give the highest drag due to its smooth contour. Hoerner[19] describes the drag rise due to various boundary-layer protrusions and indicates that protrusions with highest curvature change give rise to the highest drag rise. To modify this elastica shape into a curve that produces more drag, additional actuator forces will need to be applied normal to the airfoil skin. This means that the bump shape needs to be optimized such that sufficient drag for the production of a yawing moment is obtained, while still minimizing the actuation energy required.

The behavior of the elastica after bending, is nonlinear with respect to the elastica slope. The aerodynamic forces on the bump also continuously change with the bump shape and size. Therefore, we have a nonlinear system subject to nonconservative forces. The solution to such a problem, even in two-dimensions, is not straightforward. Because the aerodynamic forces are also nonuniform over the bump, a finite element model is applied to solve the problem. The structural analysis of the airfoil bump is done using the ANSYS™ software. A nonlinear finite element calculation is performed using frame elements. At each deformation increment in the structural analysis using ANSYS, the neural network NN-CFD is used to update the aerodynamic pressure over the bump. The ANSYS analysis is again performed using this changed aerodynamic pressure. For each load step, the displacement is determined using a Newton–Raphson iteration. This procedure is repeated until a steady state is obtained between the predicted deformation from ANSYS under the aerodynamic pressure for that deformation from the neural network. A series of such ANSYS runs is performed using a variety of actuator loading. The results obtained are used in training a neural network to represent the structural model.

Neural Network Implementation

The concept of neural networks is an attempt at an artificial simulation of the functioning of the human brain.[20] Design of a neural network consists of arranging neurons in different layers, deciding on their connectivity, defining the inputs and outputs of the system, and determining the strength of each connection in between the neurons. The strength of the neuron connections is based on training a neural network on a series of data sets. Once a neural network have been trained using sufficient data, then the network is capable of providing the desired output given a new set of input data. Optimization procedures based on neural networks have been widely used in aircraft applications.[14,21,22] In the present work, the neural network package available in MATLAB®[23] is used. The data required for training the neural network is 1) the bump parameters, size, shape, and location; 2) the aerodynamic forces, lift, drag, and static pressure over the bump; and 3) the actuation energy required, and the actuator loads. The parameterization of the bump is done using cubic splines. The B-splines that were used to model the airfoil can be used to model cubic splines as well by fixing the number of control polygon points appropriately. A single cubic spline of the form

$$y(x) = c_0 + c_1 x + c_2 x^2 + c_3 x^3$$

is used. The coefficients of the cubic spline that represent the bump are used as inputs to the neural network. The x values of the bump are normalized with respect to the bump span, so that they range between 0 and 1. The neural network is trained using the Levenberg–Marquardt algorithm. This is a variation of Gauss–Newton's method

involving a second-order Taylor's series expansion of the minimization function about an initial value. The Levenberg–Marquardt iterations proceed according to

$$y_{k+1} = y_k - (J^T J + \lambda I)^{-1} J^T e \tag{5}$$

where λ is a constant parameter and J is the Jacobian of the error e with respect to the network weights. The error, e is estimated by computing the absolute difference between the actual network output and the desired network output. The advantage of the Levenberg–Marquardt scheme is that the Jacobian matrices that are involved in the Taylor's series expansion of the minimization function are forced to be diagonally dominant for each iteration in the minimization process. This ensures faster convergence than the Gauss–Newton scheme for nonlinear data fitting. The disadvantage of the Levenberg–Marquardt scheme is that there is a limit to the data that it can handle, due to memory constraints.

In the present training procedure, the L_2 norm of the error between the target and the neural network simulation is set to 10^{-6}. The number of layers in which neurons need to be arranged and the number of neurons in each layer must be selected to obtain a good fit of the data, so that the fidelity of the trained neural network is high. The neural network output is trained to be accurate within a desired tolerance at locations away from the data points by adjusting the number of neurons in each layer and also the size of the data set.

Two neural networks are used for the aeroelastic analysis.

First the neural network NN-CFD is trained based on the data from FLUENT. The output of this neural network is the aerodynamic pressure acting on the bump. Its input is the bump shape parameters in the form of the coefficients of the cubic spline that describes the bump. The aerodynamic pressure over the bump as output by NN-CFD is used by the ANSYS package to calculate the deformation of the bump. The result of the ANSYS analysis, in the form of new bump shape parameters, is fed back to this neural network to calculate the changed aerodynamic pressure.

Second, with the use of the structural data, namely the strain energy, actuator loads, a second neural network, NN-STR is trained. This neural network has as its output the strain energy of forming the bump, the actuator loads, the lift and drag coefficients. The inputs for NN-STR are the bump shape parameters in the form of the coefficients of the cubic spline that describes the bump.

The output function of the layers and the number of neurons per layer are 1) layer 1, hyperbolic tangent sigmoid, 20 neurons; 2) layer 2, log sigmoid, 12 neurons; and 3) layer 3, purelin linear ramp function. The number of neurons depends on the number of outputs of this neural network: This was four in case of NN-CFD, representing the static pressure over the bump, and seven in the case of NN-STR, signifying the actuator loads, their location, and the lift and drag coefficients over the airfoil.

The number of neurons in each layer are determined by trial and error during the training process. These two neural networks replace the analysis performed using FLUENT and ANSYS for aerodynamics and structures, respectively.

Low-Speed Aerodynamics

For the low-speed analysis, the freestream velocity is assumed to be at Mach 0.3 and an angle of attack of 5 deg. The far-field pressure boundary conditions are specified on all of the four faces of the boundary. In FLUENT, this means that the flow velocity on the boundaries is specified along with the temperature, which allows for the calculation of the Riemann invariants (see Ref. 24). The bump is located just after the leading edge on the upper surface of the airfoil.

Initially, a study on the height of the bump is performed. The size of the bump is blown up from a y coordinate value of 0.2% of the airfoil chord to a value of 0.4% of the airfoil chord. The accuracy of the CFD analysis is known from the convergence of the residuals for the flow variables, as shown in Fig. 3. In this case, that is, with a bump height of 0.2% of the airfoil chord, the flow has not separated completely, and hence, a steady solver is used. The residuals computed are based on rms value of the time rate of change of the conserved variable. Figure 3 shows that the residuals for the density and velocities have converged to within 10^{-5}.

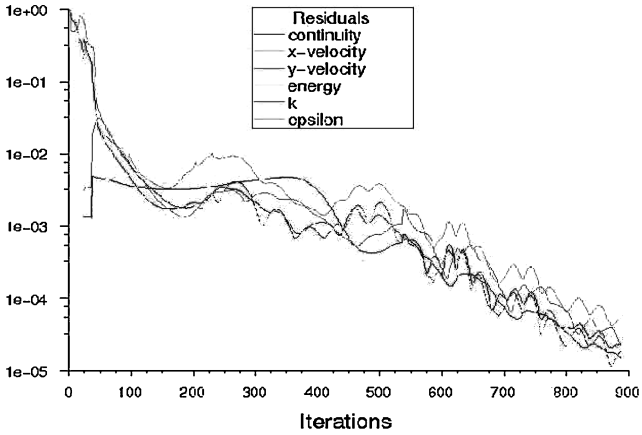

Fig. 3 Scaled residuals of the flow variables as computed by FLUENT showing the convergence of the finite volume scheme.

Figure 4 shows the velocity magnitude contours. It can be seen that, beyond a bump size of the order of 0.35% of the chord, there is a total separation of the flow. However, as the bump height is further increased, as seen in Fig. 4c, there is a reattachment of the flow after an initial separation at the bump. This reattached flow is not stable and separates after a zone of attached turbulent flow. Both from the point of view of actuation energy and of aircraft control, it is necessary to confine the bump size to the region of predictable separation. This means that the required bump height is of the order of 0.35% of the airfoil chord. Because the purpose of having this bump is to provide a yaw control mechanism, whether the drag produced by the specified bump size is sufficient it needs to be determined. At the same time, the lift generated by the airfoil should not be seriously reduced. Figure 5 shows the effect of the same type of bump as in Fig. 4, but at a location farther down the airfoil. In Fig. 4, the bump was at a location of $x/c = 0.4\%$, whereas in Fig. 5, the bump is at a location, of $x/c = 3.8\%$.

Figure 6 shows the variation in the lift coefficient and the drag coefficient with bump size. After a certain bump height, oscillatory patterns are observed in the coefficient of lift. It is seen that sufficient drag for yaw moment can be achieved without serious deterioration in the lift and that there is a fixed bump height above which the lift and drag forces are highly oscillatory. We say that the decrement in lift is not substantial because we are speaking of morphing wings, wings for which this loss in lift can be overcome with some adaptive cambering of wing sections at different locations where the flow does not separate. At a drag coefficient of 0.012, that is, at a bump height of 0.085 cm, or 0.35% of the chord, the drop in the lift is less than 10%. Above the bump height of 0.35% of the chord, the drag and lift forces are oscillatory with respect to further increase in bump height. This is because of the reattachment phenomena and further separation after reattachment. This flow regime is also highly unsteady due to vortex shedding. Hence, as can be seen from Figs. 4–6, the maximum height of the elastica, that is, deformed by the actuator, is of the order of 0.35% of the airfoil chord. Using Eq. (1) with a section drag coefficient of 0.02 and wing properties as span is equal to 20 m, root chord is equal to 8 m, tip chord is equal to 2 m, and aspect ratio is equal to 4.0, and assuming a somewhat flexible wing material, the material properties are $E = 7000$ MPa and $\nu = 0.3$, and the yaw moment coefficient can be estimated as $C_n = 0.002$. As mentioned earlier, this C_n is comparable to those estimated in Refs. 5 and 6.

High-Speed Aerodynamics

Typically the adaptable bumps that have been the subject of widespread investigation, as mentioned earlier,[5,6] have been to study wave drag reduction. Therefore, we investigate a flow speed of Mach 0.7 over the same 8% thick airfoil. Figure 7 shows the velocity magnitude contours over the airfoil. Figure 7a shows the airfoil with no

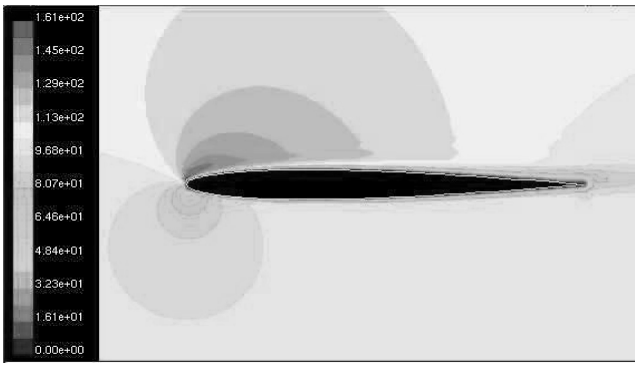

a) Leading-edge bump height 0.2% chord

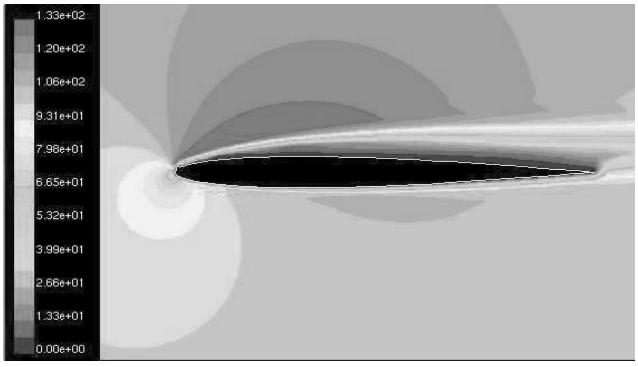

b) Leading-edge bump height 0.35% chord

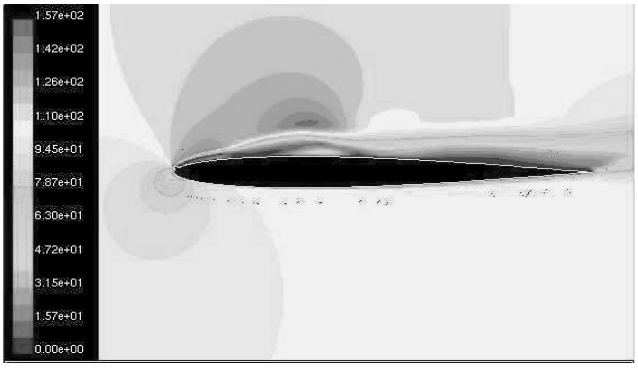

c) Leading-edge bump height 0.4% chord

Fig. 4 Velocity contours showing separation at freestream velocity of Mach 0.3.

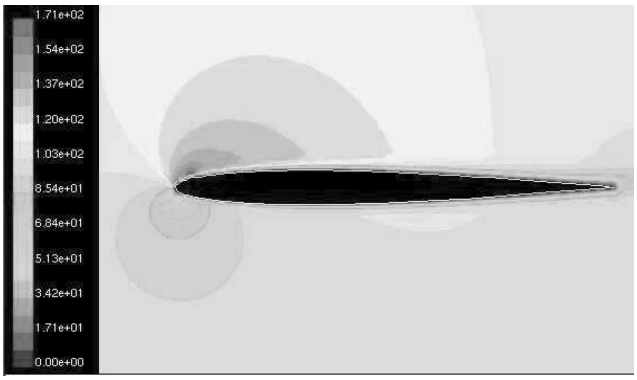

a) Turbulent boundary layer

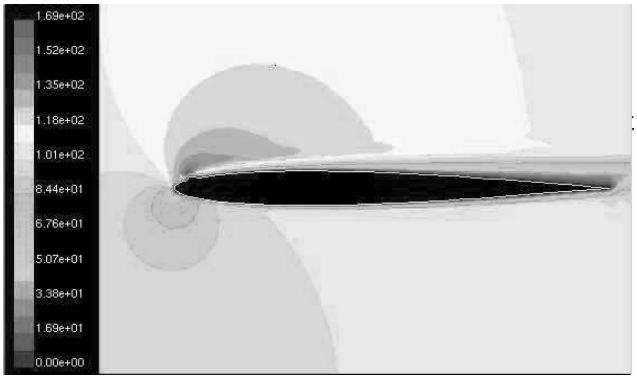

b) Onset of boundary-layer separation

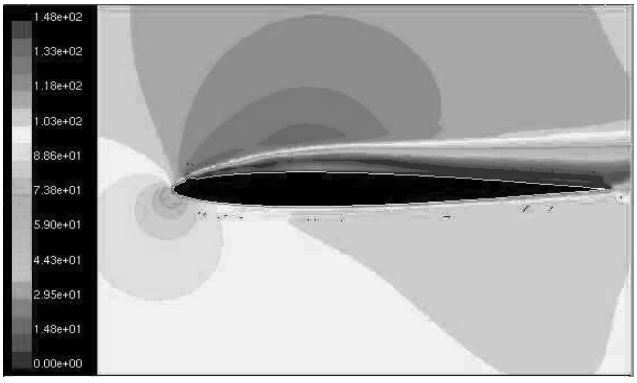

c) Fully separated flow

Fig. 5 Velocity contours showing fluid separation at a freestream velocity of Mach 0.3 from a bump at 3.8% of the chord.

leading edge bump. A strong shock is seen over the airfoil. This naturally leads to a substantial wave drag. Now an adaptive bump is grown at a location of $x/c = 0.4\%$. Figures 7b and 7c show the velocity contours at bump heights at 0.1, 0.2, and 0.28% of the airfoil chord. Note that the shock is weakened significantly. At a bump height of 0.2% of airfoil chord, there is boundary-layer separation. On further increase of the bump height to 0.28%, the shock is completely lost, and total boundary-layer separation is seen. From the point of view of actuation energy required to produce this bump, it can be seen that a very small bump size is enough to nullify the shock. In contrast, typical wave drag minimization bumps have been situated near the edge of the shock, toward the trailing edge with a maximum bump size of 0.5% of the airfoil chord.[7] This limit on the bump size to 0.5% of the chord is to prevent boundary-layer separation.

Low-Speed Aeroelastic Optimization

The optimization is initiated based on the bump shapes used to train the neural networks, a sample of which is shown in Fig. 8. A segment of the leading edge of the airfoil is subjected to fluid dynamic pressure, a compressive axial load and an arbitrary vertical load, leading to the formation of a bump. The axial and vertical loads are the actuator loads. Figure 9 shows the freebody diagram of the bump as a curved beam subjected to an axial compressive load, B, aerodynamic pressure, P and an arbitrary load T. The load T is arbitrary in the sense that its direction and magnitude, as well as its location, need to be fixed by the optimization process. The beam length is small, being 1.3% of the chord in the case of low-speed flow and 3.5% of the chord in case of high-speed flow.

With use of the aerodynamic results from FLUENT, the neural network, NN-CFD, capable of predicting the fluid static pressure at four points over the bump, was trained for various bump shapes. The static pressures calculated by the neural network are inputs to the ANSYS structural analysis of the bump. When ANSYS is used, both the actuator loads and the strain energy required for deforming the bump are obtained. These actuator loads, their position, and the strain energy of deformation are used as targets for the second neural network, NN-STR. The aerodynamic drag and lift over the

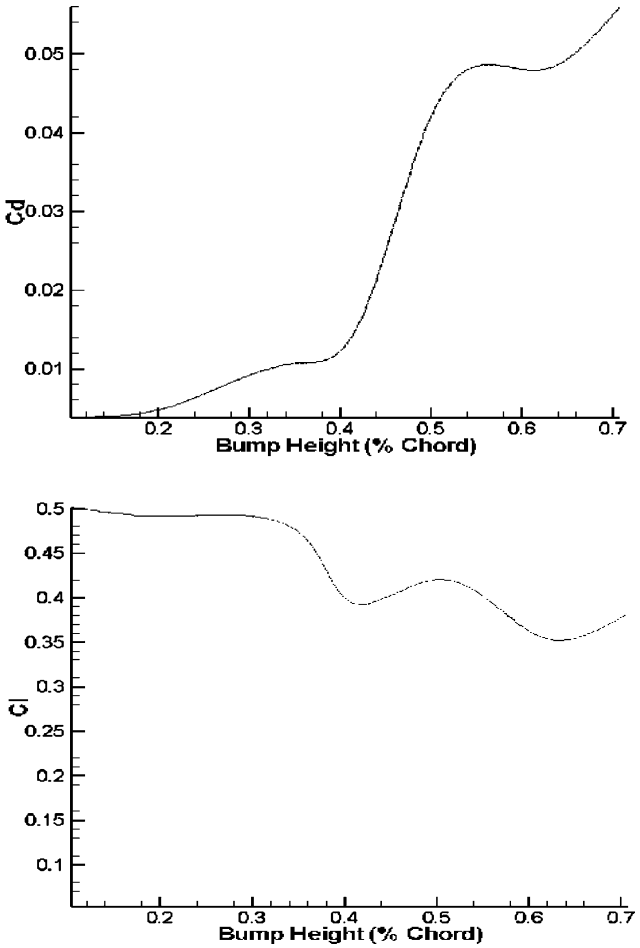

Fig. 6 Effect of size of a bump located at 3.8% chord on the drag and lift at a freestream velocity of Mach 0.3.

airfoil are also used as targets for NN-STR. This means that this neural network will be able to predict the strain energy, actuator loads, and lift, and drag over the airfoil given the coefficients of a cubic spline fit to the bump as its input. Figure 10 is a flow chart that describes the process of training the neural networks for obtaining the structural loads and energy for deformation of the bump and the fluid dynamic pressure over the bump along with the aerodynamic lift and drag. The training time for a given set of data and target points in MATLAB is about 10 min. However, further testing, possible network reorientation, and further training may be required to obtain the desired network fidelity. A similar training procedure is used for the network NN-STR based on the ANSYS and FLUENT results. The trained neural networks are then stored in binary files. These trained neural networks are used for optimizing the bump shape.

Compressive axial actuator loads, vertical actuator loads, and aerodynamic pressure act on the bump causing it to deform. As mentioned earlier, we need to maximize the drag created due to the presence of the bump while minimizing the actuation energy needed to create this bump. The constraint on the bump creation is that minimal loss in lift is desired. We formulate the optimization problem as follows.

Minimize

$$1\Big/c_d^2 + G \times (c_l - 0.47)^2 + G_2 \times \kappa^2 \tag{6}$$

subject to C_0 continuity between bump and the airfoil, where c_l and c_d are the coefficients of lift and drag, respectively; κ is the scaled strain energy, which is scaled with respect to the largest deformation strain energy; and G and G_2 are two penalty weights, selected by trial and error depending on the rate of minimization of the objective function and also the C_0 continuity between the bump and the airfoil.

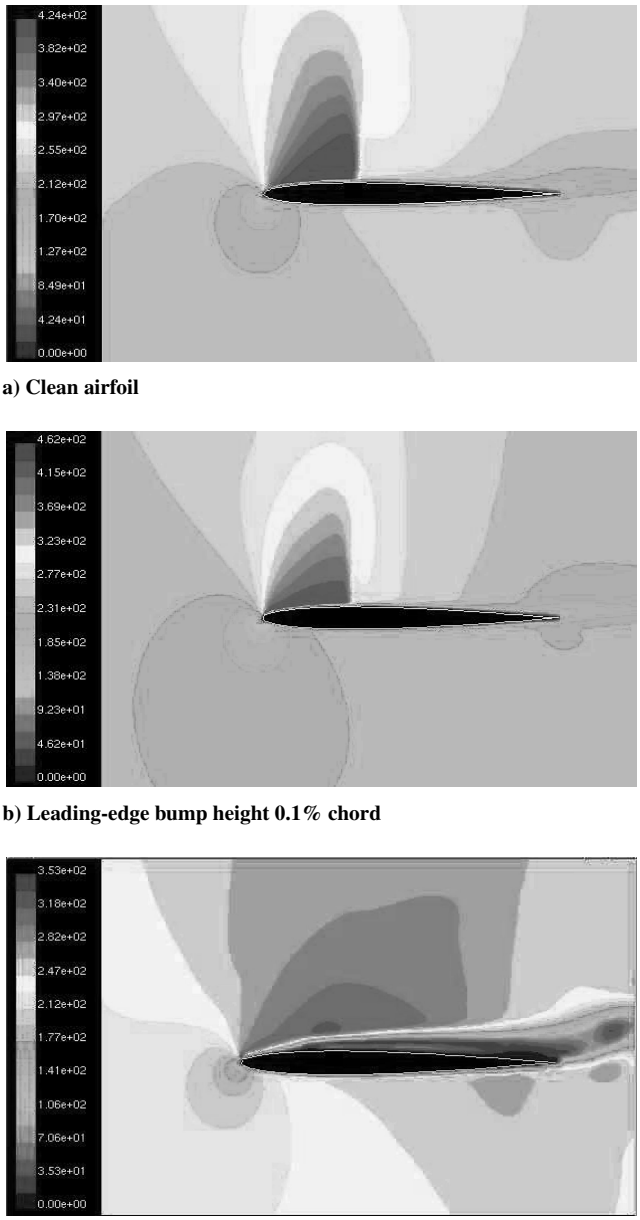

a) Clean airfoil

b) Leading-edge bump height 0.1% chord

c) Leading-edge bump height 0.28% chord

Fig. 7 Velocity contours generated using FLUENT showing the effect of the bump size on the shock and the boundary layer (freestream Mach number 0.7).

This problem is schematically represented in the flow chart shown in Fig. 11.

This optimization problem requires the solution of five geometric variables, that is, the four coefficients of the single cubic spline that represents the bump and the location of the one end of the cubic spline, which is free to move under the imposed loads. The optimization problem requires the solution of four structural parameters, which are the magnitude of the axial load, and the magnitude, direction, and location of the transverse actuator load. The optimization also solves for two aerodynamic parameters, which are the coefficient of lift and the coefficient of drag over the airfoil. Hence, even though the angle of attack is held constant at 5 deg, the optimization problem still requires the computation of many variables using a multidisciplinary analysis.

The optimization is performed using the conjugate-gradient method. Let $\boldsymbol{d}(n)$ be the direction vector of the nth iteration of the conjugate-gradient scheme. The initial direction vector, $\boldsymbol{d}(0)$, is set equal to the negative gradient vector, $\boldsymbol{g}(0)$ at the initial point $n = 0$. Successive direction vectors are then computed as a linear combination of the current negative gradient vector and the previous

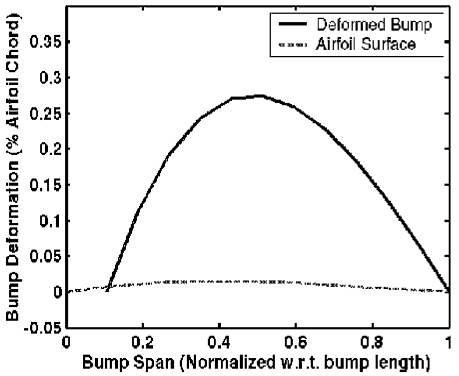

a) Bump A

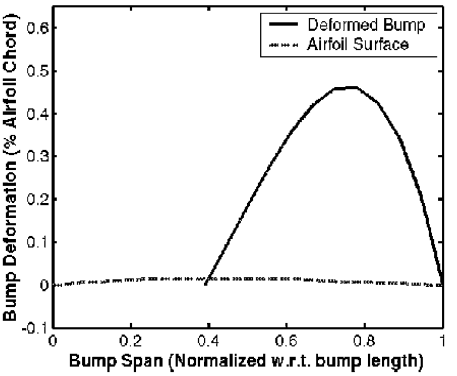

c) Bump C

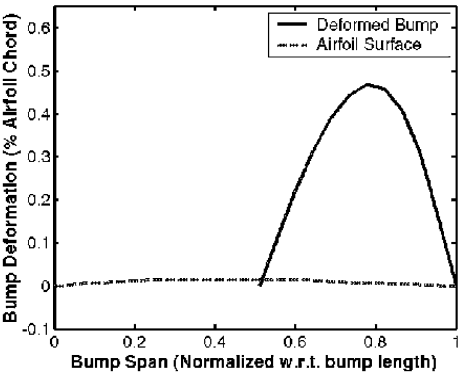

b) Bump B

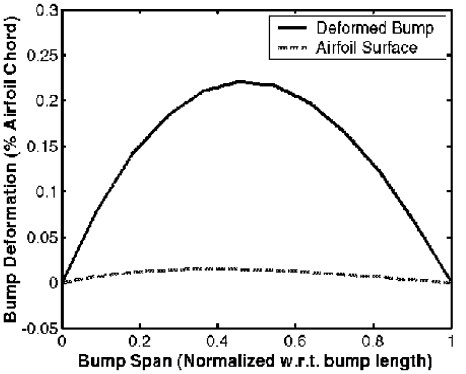

d) Bump D

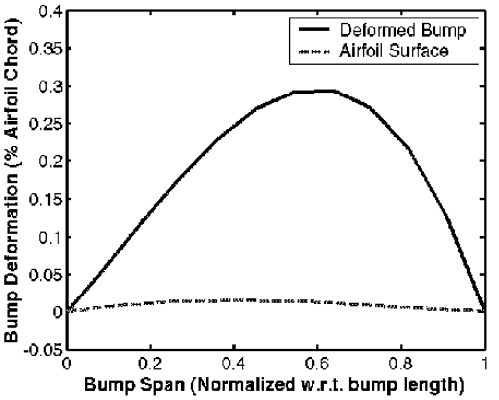

e) Bump E

Fig. 8 Various bump shapes used for training neural networks to represent the aerodynamic load over the bump.

direction vector as

$$\boldsymbol{d}(n+1) = -\boldsymbol{g}(n+1) + \beta(n)\boldsymbol{d}(n) \tag{7}$$

where β is a parameter that ensures that the new search direction is orthogonal to the previous search direction. Note that β can be computed using many techniques, a popular one being, the Fletcher–Reeves formula,

$$\beta(n) = \frac{[\boldsymbol{g}^T(n+1)\boldsymbol{g}(n+1)]}{[\boldsymbol{g}^T(n)\boldsymbol{g}(n)]} \tag{8}$$

Since this problem is nonlinear, the number of iterations for convergence for the conjugate-gradient method is not fixed. The C_0 boundary conditions for the bump are fixed by imposing a penalty on the objective function to be minimized. Since the conjugate-gradient method requires the calculation of the Jacobian and Hessian matrices, a finite difference approximation for the derivatives at each point in the iteration is calculated. At each step in the iteration, the neural network NN-STR simulates the new actuator loads, strain energy, and resulting drag and lift over the airfoil. The optimum value for the bump shape that is obtained from the neural network may be a local optimum. The optimization is repeated for a set of bumps with new initial aerodynamic and structural parameters, where the aerodynamic parameters are the drag and lift and the structural parameters are the actuator loads and the strain energy.

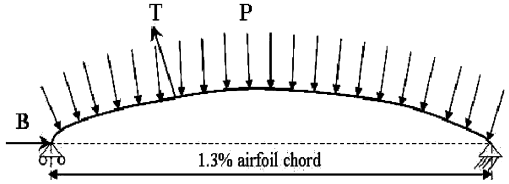

Fig. 9 Freebody diagram of the bump as a beam under axial and transverse loading.

Among this calculated set of optimal solutions, the best solution is that which approaches the design lift constraint of 0.47

and still provides a drag coefficient of at least 10^{-2}. The calculated bump shapes that minimize the objective function is shown in Fig. 12. The neural network was trained based on bump shapes similar to those shown in Fig 8. Therefore, one can conclude that, of all bump shapes that fall within the range of the bumps described in Fig. 8, the bump shapes shown in Fig. 12 minimize the strain energy and retain maximum drag and minimum loss in lift. The latter criterion, that is, minimum loss in lift, is significant. The created airfoil surface bump, not only provides for drag sufficient for yaw control, but also allows for a minimum loss in lift such that it can be compensated by slight cambering of a different wing section. Because the neural network NN-STR is capable of simulating the aeroelastic interactions of the bump, we have a rapid two-dimensional static aeroelastic optimization tool.

The three bump shapes shown in Fig. 12 detail the optimum shapes for minimal loss in lift. As given by Eq. (2), we require that the lift should not be drastically reduced below a value of 0.47. The drag and lift coefficient values are given with Figs. 12a–12c. Because of the limitations of the neural network training, the predicted values of drag and lift using the neural network are 10% less than the corresponding CFD results.

1) Figures 12a shows a bump that was formed without any axial load. The bump has only a vertical actuator load at its center. As shown, there is a moderate drag increase without substantial loss in lift.

2) Both Figs. 12b and 12c show bumps formed with axial and transverse actuator loads. A moderate drag increase without serious loss in lift is obtained from the bumps. From the obtained drag, lift, and strain energy for the bumps shown in Fig. 12, it can be

Table 1 Comparison of optimized results with those used in training[a] (Ref: Fig. 8)

	Bump shapes used in training					Optimized shapes		
Parameter	A	B	C	D	E			
Strain energy, J/cm thickness	17.24	91.536	89.43	25.71	133.09	115.704	128.628	109.64
C_d	0.0174	0.039	0.0274	0.0078	0.018	0.0227	0.0222	0.0245
C_l	0.453	0.3689	0.414	0.4771	0.4686	0.4559	0.4393	0.4476
Axial load, N	4000	9012	4000	0	0	0	1566	1086
X load, N	−5000	0	3000	0	−30000	0	−28110	−3582
Y load, N	8000	0	20000	19000	60000	50010	64950	60990
Position of X–Y load, % span	18	0	70	45	73	45	19.94	47.92

[a]Clean airfoil: $C_d = 0.005$ and $C_l = 0.52$.

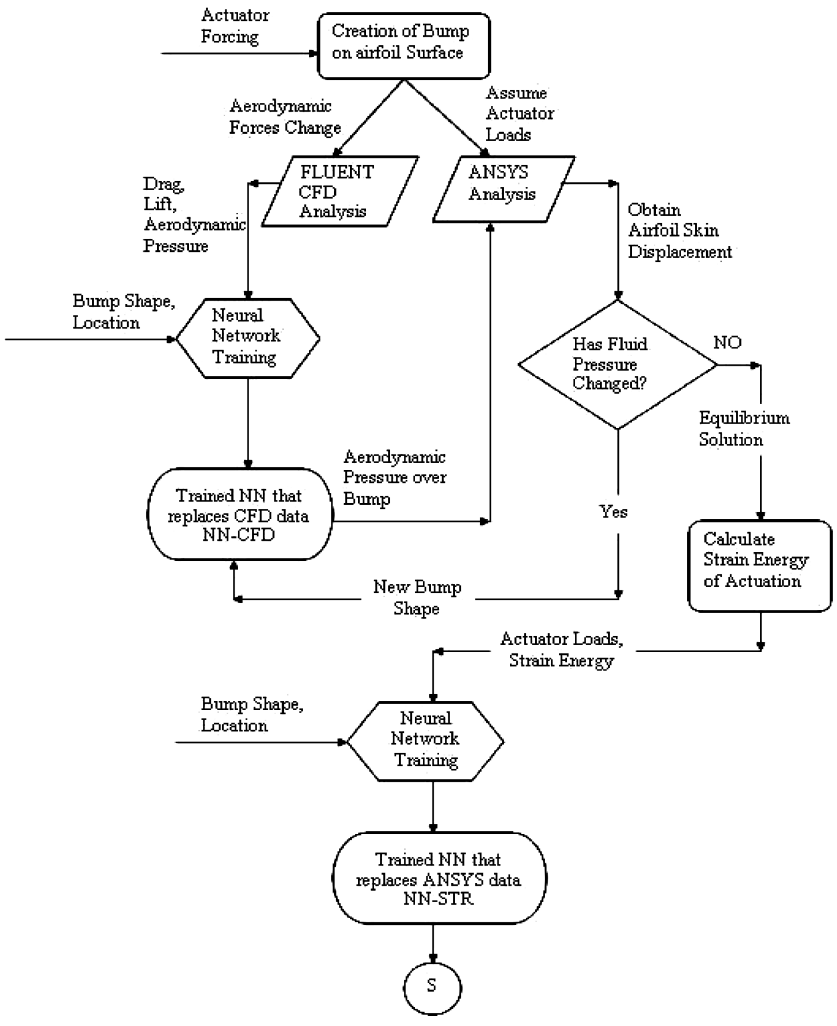

Fig. 10 Process of evaluating the aeroelastic response of the bump by training two neural networks.

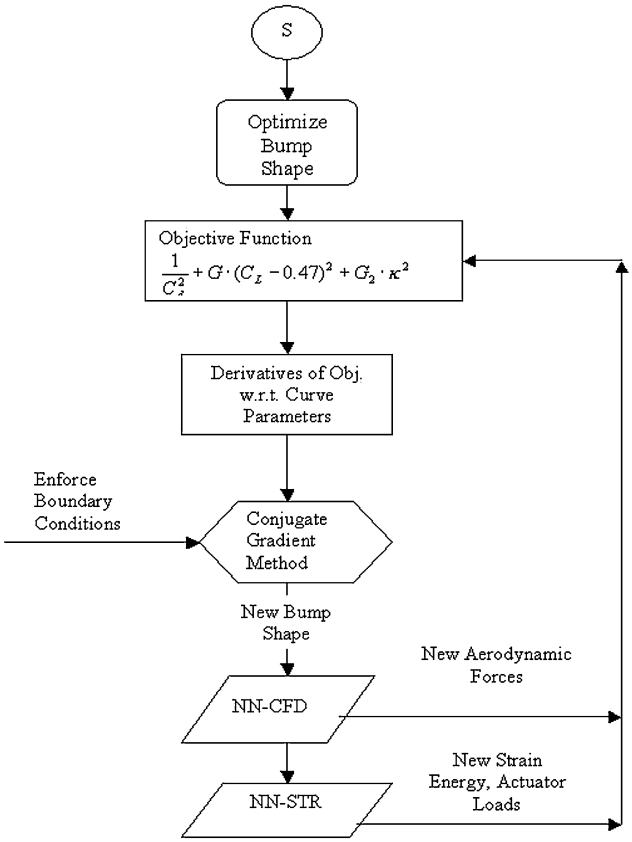

Fig. 11 Process of optimizing the bump shape using the trained neural networks.

said that Fig. 12b describes the optimum bump shape amongst the set of bumps that can be generated from the beam model shown in Fig. 9. Table 1 shows a comparison of the optimized results with other bumps such as those shown in Fig. 8, which were used for training the neural networks.

A drag coefficient of the order of 0.02 is attainable without serious loss in lift and by minimizing the strain energy required for forming the bump. The clean airfoil obtains a lift coefficient of 0.51 at 5-deg angle of attack. Therefore, there are lift losses of the order of 11%. However, because we are dealing with an adaptable wing, the wing can possess adaptive cambering at a section different from wing section that has a bump. Even a 1% camber increase at 60–70% of the chord is enough to offset the decrement in lift due to the bump.

High-Speed Aeroelastic Optimization

For the freestream flow velocity of Mach 0.7, Fig. 7 shows the effect of the leading-edge bump on the shock, as well as the boundary layer. The same realizable k–ϵ model was used, as in the low-speed case. This turbulence model may not be adequate for such high-speed flows, but due to limits in computational time, a more advanced model such as the five-equation Reynold's stress model could not be used. This can be a topic of future research work, that is, significance of turbulence models on aeroelastic analysis. As described earlier, a very small perturbation (of the order of 1% of the chord) decreases the wave drag. A further increase in the bump size leads to flow separation. From the actuator point of view, the main factor of concern here is the rapidly changing aerodynamic pressure over the bump with small perturbations in the bump height. The length of the bump in the low-speed analysis allows the beam model to possess greater flexibility than that permissible under a high-speed flow. The shorter the bump length, the stiffer is the bump. The leading-edge bump could not be used for high-speed flow because a steady-state bump equilibrium is difficult to achieve. Also the drastic changes in pressure over the bump with

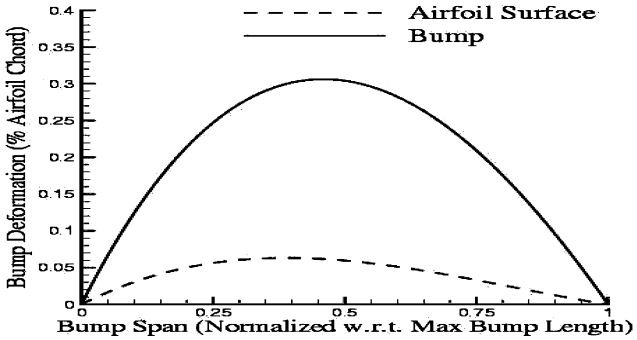

a) $C_d = 0.0227$, $C_l = 0.4543$, and strain energy = 115.7 J/cm thickness

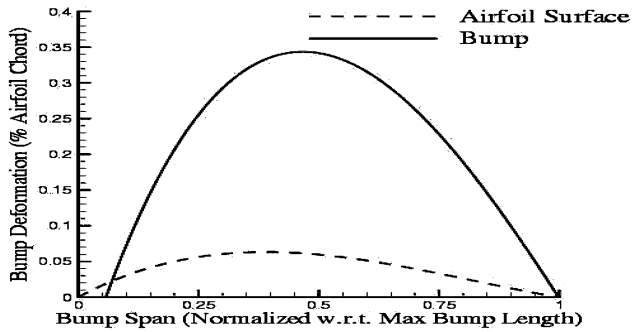

b) $C_d = 0.0245$, $C_l = 0.456$, and strain energy = 109.6 J/cm thickness

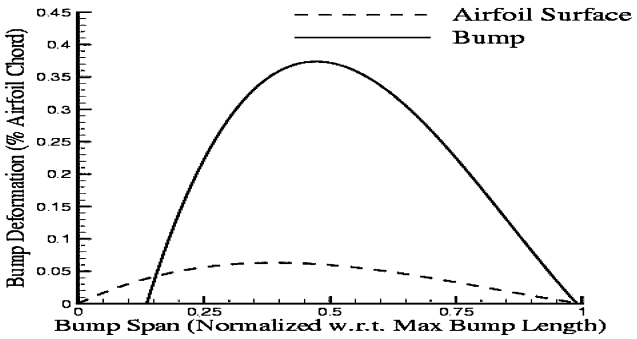

c) $C_d = 0.0222$, $C_l = 0.4393$, and strain energy = 128.4 J/cm thickness

Fig. 12 Optimized bump shapes for freestream velocity of Mach 0.3.

minute changes in bump shape could not be captured by the neural network.

Because our concern is not with shock control, the bump is placed downstream of the shock. This allows for choosing a bump shape that is not drastically affected by changing aerodynamic pressure. Even then, the low pressure on the bump, does not allow for axial compression, unlike the low-speed model. This is because the beam model of the bump is now susceptible to buckling at very low axial loads. Hence, a pinned–pinned beam is considered subjected to an arbitrarily oriented load at any arbitrary position.

As was done in the case of low-speed, 14–15 runs were performed in FLUENT and ANSYS to collect sufficient data to train the neural networks, NN-CFD and NN-STR. The trained neural networks are then used to optimize the bump shape that provides maximum drag with a minimum loss in lift and minimum strain energy required to form the bump. Figure 13 shows the effect of bump on the shock and the boundary layer. It can be seen that the amount of separation generated is lesser than the low-speed case. This means that the amount of drag increase is also less. The effect of the bump on the shock is also seen in Fig. 13. Compared to Fig. 8, Fig. 13 shows that a much larger bump size is required to cause a full weakening of the shock. The height of the bump in Fig. 13c that shows the weakened shock is of the order of 0.92% of the airfoil chord.

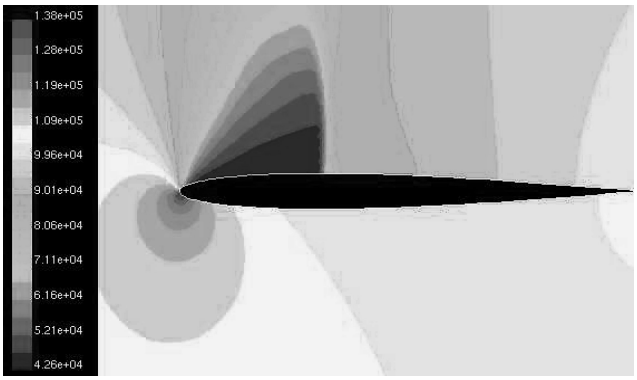

a) Clean airfoil, $C_d = 0.0433$ and $C_l = 0.717$

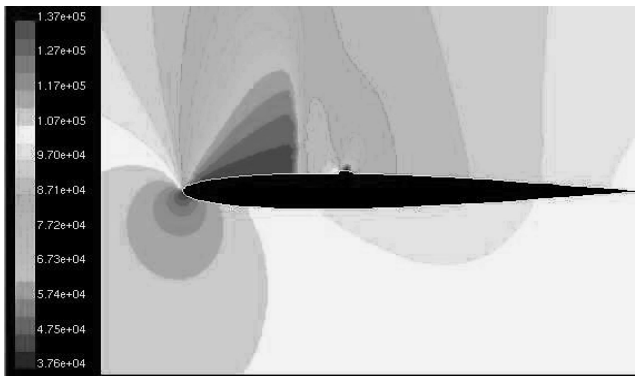

b) $C_d = 0.0482$, and $C_l = 0.632$

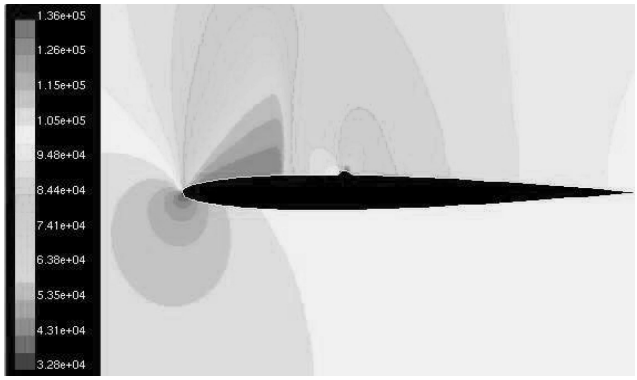

c) $C_d = 0.0536$, and $C_l = 0.613$

Fig. 13 Static pressure contours at freestream velocity of Mach 0.7.

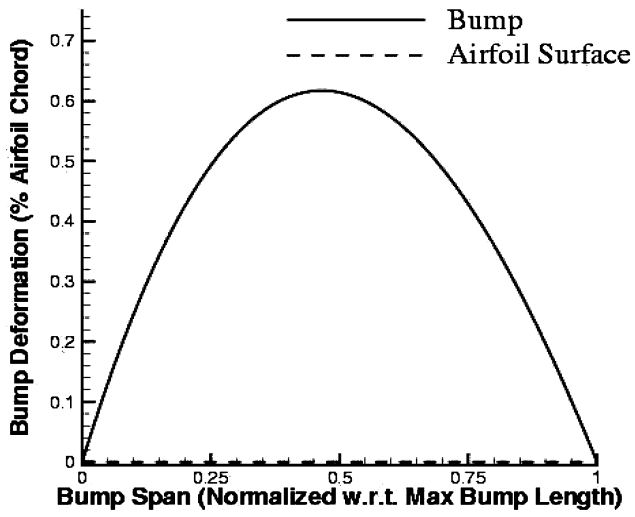

a) $C_d = 0.0498$, $C_l = 0.681$, and strain energy = 104 J/unit cm thickness

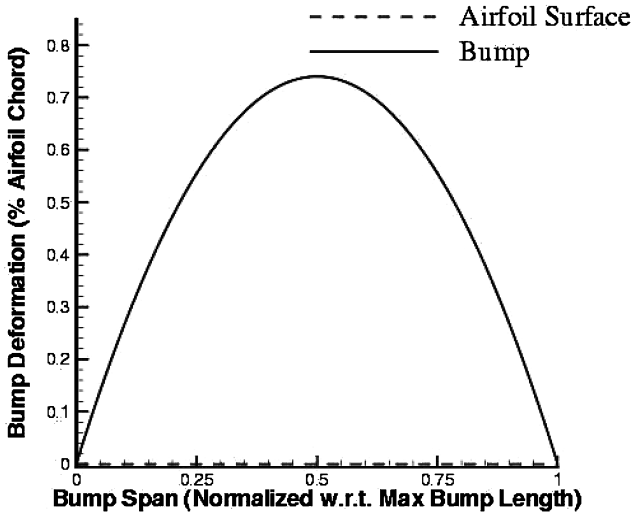

b) $Cd = 0.0519$, $Cl = 0.653$, and strain energy = 198.5 J/unit cm thickness

Fig. 14 Optimized bump shapes for freestream velocity of Mach 0.7.

The objective function is the same as was used for the low-speed case, that is, Eq. (6), but the lift coefficient was fixed at 0.63 to account for the compressibility. The bump shapes that minimize this objective function are shown in Fig. 14. Again, many initial conditions were tried to select the best optima. The two best bump shapes are shown in Fig. 14 and result in 1) a moderate pressure drag coefficient increase of 0.005 but with a low loss in the lift and low 21 strain energy required to form the bump (Fig. 14a) and 2) a significant drag increase at high speeds and with a low loss in the lift and moderate strain energy required to form the bump as shown in Fig. 14b. These two bump shapes can be selected depending on the amount of drag that is required.

Conclusions

A neural-network-based approach for aeroelastic optimization of bumps on morphing wings has been demonstrated. The case study that was performed was the selection of an optimum bump shape on an airfoil surface that leads to controlled flow separation that can be used in generating sufficient yawing moment for a morphing wing aircraft. With use of the CFD code FLUENT, the aerodynamic

forces over the airfoil and static pressure over the adaptive bump are computed for several bump shapes. The actuator forces and energy required in creating these bumps is calculated using the finite element software ANSYS. With these results, a database is formed, which is used in training two neural networks. The first neural network provides the static pressure over the bump given any bump shape, and thus, this neural network replaces FLUENT calculations. The second neural network provides the actuation forces and energy required in creating the bump, as well as the drag and lift over the airfoil, thus, replacing both FLUENT and ANSYS analysis. This facilitates a rapid calculation of aeroelastic behavior of the airfoil bump.

A conjugate-gradient scheme used in conjunction with the two trained neural networks allows the aeroelastic optimization of the adaptable bumps at speeds of Mach 0.3 and Mach 0.7. The study revealed the sensitivity of the flow to the bump shape, size, and location. A set of bump shapes that minimize the objective function were obtained such that sufficient yaw moment is generated. This analysis was performed in two dimensions, and the work demonstrates the use of neural networks in the nonlinear aeroelastic analysis of morphing wings. A three-dimensional analysis can account for variations in bump shape along the spanwise direction, as well as variations in the angle of attack. More investigations need to be done on using decision making systems such as neural networks for representing the aeroelastic behavior of flexible structures. A clear representation of the aeroelastic behavior of a morphing wing through neural networks speaks of a high potential in the design of an active aeroservoelastic flight control system.

Acknowledgment

The authors gratefully acknowledge the support of AFOSR grant F49620-99-1-0294, monitored by B. Sanders, Ph.D. of AFRL and E. Garcia of DARPA.

References

[1]Khot, N. S., Zweber, J. V., Veley, D. E., Oz, H., and Eastep, F. E., "Flexible Composite Wing with Internal Actuation for Roll Maneuver," *Journal of Aircraft*, Vol. 39, No. 4, 2002, pp. 521–527.

[2]Barrett, R., "All-Moving Active Aerodynamic Surface Research," *Journal of Smart Materials and Structures*, Vol. 4, No. 4, 1995, pp. 65–74.

[3]Campanile, L. F., and Sachau, D., "The Belt Rib Concept: A Structronic Approach to Variable Camber," *Journal of Intelligent Material Systems and Structures*, Vol. 11, No. 3, 2000, pp. 215–224.

[4]Gern, F. H., Inman, D. J., and Kapania, R. K., "Structural and Aeroelastic Modeling of General Planform UCAV Wings with Morphing Airfoils," *AIAA Journal*, Vol. 40, No. 4, 2002, pp. 628–637; also *42nd AIAA/ASME/ASCE/AHS/ASC Structures, Structural Dynamics and Materials Conference*, AIAA Paper 2001-1369, April 2001.

[5]Stanewsky, E., "Aerodynamic Benefits of Adaptive Wing Technology," *Aerospace Science and Technology*, Vol 4, No. 7, Sept. 2000, pp. 439–452.

[6]Bein, T. H., Hanselka, H., and Breitbach, E., "Adaptive Spoiler to Control the Transonic Shock," *Smart Materials and Structures*, Vol. 9, No. 2, 2000, pp. 141–148.

[7]Gano, S. E., and Renaud, J. E., "Optimized Unmanned Aerial Vehicle withWing Morphing for Extended Range and Endurance," *9th AIAA/ISSMO Symposium and Exhibit on Multidisciplinary Analysis and Optimization*, AIAA Paper 2002-5668, Atlanta, GA, Sept. 2002.

[8]Ashkenas, L. I., and Klyde, D. H., "Tailless Aircraft Performance Improvements with Relaxed Static Stability," NASA CR 181806, March 1989.

[9]Northrop, J. K., "The Development of the All Wing Aircraft," *Journal of the Royal Aeronautical Society*, 35th Wilbur Wright Memorial Lecture, Vol. 51, 1947, pp. 481–510.

[10]Moul, T. M., Fears, S. P., Ross, H. M., and Foster, J. V., "Low-Speed Wind-Tunnel Investigation of the Stability and Control Characteristics of a Series of Flying Wings With Sweep Angles of 60 Degrees," NASA TM-4649, Aug. 1995.

[11]Cole, S. R., "Aeroelastic Effects of Spoiler Surfaces on a Low-Aspect Ratio Rectangular Wing," *Journal of Aircraft*, Vol. 29, No. 5, 1992, pp. 768–773.

[12]Pinkerton, J. L., and Moses, R. W., "A Feasibility Study to Control Airfoil Shape Using THUNDER," NASA TM 4767, Nov. 1997.

[13]Faller, W. E., and Schreck, S. J., "Unsteady Fluid Mechanics Applications of Neural Networks," *Journal of Aircraft*, Vol. 34, No. 1, 1997, pp. 48–55.

[14]Rai, M. M., and Madavan, N. K., "Aerodynamic Design Using Neural Networks," *AIAA Journal*, Vol. 38, No. 1, 2000, pp. 173–182.

[15]Bauer, S. X. S., "An Aerodynamic Assessment of Micro-Drag Generators (MDGs)," *16th AIAA Applied Aerodynamics Conference*, AIAA Paper 98-2621, Albuquerque, NM, June 1998.

[16]Raney, D. L., and Park, M. A., "Flight Control Using Distributed Shape-Change Effector Arrays." *41st AIAA/ASME/ASCE/AHS/ASC Structures, Structural Dynamics, and Materials Conference*, AIAA Paper 2000-1560, Atlanta, GA, April 2000.

[17]Shih, T. H., Liou, W. W., Shabbir, A., and Zhu, J., "A New k–ϵ Eddy-Viscosity Model for High Reynolds Number Turbulent Flows—-Model Development and Validation," *Computers and Fluids*, Vol. 24, No. 3, 1995 pp. 227–238.

[18]Qu, R., and Ye, J., "Efficient Approximation of Minimum Energy Curves with Interpolatory Constraints," *Applied Mathematics and Computation*, Vol. 109, No. 2–3, 2000, pp. 151–166.

[19]Hoerner, S. F., *Fluid-Dynamic Drag*, published by the author, Hoerner Fluid Dynamics, P.O. Box 21992, Bakersfield, CA, 1965.

[20]Haykin, S., *Neural Networks: A Comprehensive Foundation*, 2nd ed., Prentice–Hall, Upper Saddle River, NJ, 1999, Chap. 1, pp. 2–28.

[21]Liu, Y., and Kapania, R. K., "Equivalent Skin Analysis of Wing Structures Using Neural Networks," *AIAA Journal*, Vol. 39, No. 7, 2001, pp. 1390–1399; also AIAA Paper 2000-4802, Sept. 2000.

[22]Greenman, R. M., and Roth, K. R., "Minimizing Computational Data Requirements for Multi-Element Airfoils Using Neural Networks," *Journal of Aircraft*, Vol. 36, No. 5, 1999, pp. 777–784.

[23]Ham, F. M., and Kostanic, I., *Principles of Neurocomputing for Science and Engineering*, McGraw–Hill, New York, 2001.

[24]Tannehill, J. C., Anderson, D. A., and Pletcher, R. H., *Computational Fluid Mechanics and Heat Transfer*, 2nd ed., Taylor and Francis, Philadelphia, 1997, pp. 355–358.